

Research Article

Peridynamic Open-Hole Tensile Strength Prediction of Fiber-Reinforced Composite Laminate Using Energy-Based Failure Criteria

Xiao-Wei Jiang,¹ Hai Wang ,¹ and Shijun Guo²

¹School of Aeronautics and Astronautics, Shanghai Jiao Tong University, Shanghai, China

²Centre of Aeronautics, Cranfield University, Cranfield, UK

Correspondence should be addressed to Hai Wang; wanghai601@sjtu.edu.cn

Received 29 October 2018; Accepted 6 December 2018; Published 20 January 2019

Academic Editor: Michele Zappalorto

Copyright © 2019 Xiao-Wei Jiang et al. This is an open access article distributed under the Creative Commons Attribution License, which permits unrestricted use, distribution, and reproduction in any medium, provided the original work is properly cited.

In the present study, peridynamic (PD) open-hole tensile (OHT) strength prediction of fiber-reinforced composite laminate using energy-based failure criteria is conducted. Spherical-horizon peridynamic laminate theory (PDLT) model is used. Energy-based failure criteria are introduced into the model. Delamination fracture modes can be distinguished in the present energy-based failure criteria. Three OHT testing results of fiber-reinforced composite laminate are chosen from literatures and used as benchmarks to validate the present PD composite model with energy-based failure criteria. It is shown that the PD predicted OHT strength fits the experimental results quite well. From the predicted displacement field, the fracture surface can be clearly detected. Typical damage modes of composite, fiber breakage, matrix crack, and delamination, are also illustrated in detail for each specimen. Numerical results in the present study validate the accuracy and reliability of the present PD composite model with energy-based failure criteria.

1. Introduction

Peridynamics (PD) is found to have great advantages in dealing with fracture and damage problems in recent years [1]. Peridynamic theory of solid mechanics is established by Silling et al. [2–4]. It is a nonlocal extension of classical continuum mechanics using spatial integral equations instead of spatial differential equations. The nonlocal and integral features of PD provide a new roadmap for treating discontinuities in fracture and damage problems. Spontaneous crack propagation path can be easily realized in PD without any special treatment of the crack tip [3].

Fracture and damage of fiber-reinforced composite (FRC) is a good application area of peridynamics. Fiber breakage, matrix crack, delamination, and the interaction of these damage modes in FRC can cause many discontinuities. Fracture and damage analysis of FRC composite using PD is emerging. Askari et al. [5] analyzed the damage and failure of composite panels under static and dynamics loads. Xu et al. [6, 7] predicted in detail the delamination and matrix

damage process in composite laminates under biaxial loads and low-velocity impact. Kilic et al. [8] predicted the damage in center-cracked laminates with different fiber orientations. Oterkus et al. [9] present an approach based on the merger of classical continuum theory and peridynamic theory to predict failure simulations in bolted composite lap joints. Hu et al. [10, 11] proposed a homogenization-based peridynamic model for simulating fracture and damage in fiber-reinforced composites and analyzed the dynamic effects induced by different types of dynamic loading. Oterkus and Madenci [12, 13] present an application of PD theory in the analysis of fiber-reinforced composite materials subjected to mechanical and thermal loading conditions. Damage growth patterns of preexisting crack in fiber-reinforced composite laminates subjected to tensile loading are computed. Oterkus et al. [14] present an analysis approach based on a merger of the finite element method and the peridynamic theory. The validity of the approach is established through qualitative and quantitative comparisons against the test results for a stiffened composite curved panel with a central slot under combined internal pressure and axial tension. Hu

et al. [15] developed a PD composite model that accounts for the variation of bond *micromodulus* based on the angle between the bond direction and fiber orientation. As an extension of this model, Hu et al. [16] developed an energy-based approach to simulate delamination under different fracture mode conditions. Furthermore, Hu and Madenci [17] present a new bond-based peridynamic modeling of composite laminates without any limitation to specific fiber orientation and material properties in order to consider arbitrary laminate layouts. Sun and Huang [18] proposed a peridynamic rate-dependent constitutive equation and a new interlayer bond describing interlayer interactions of fiber-reinforced composite laminate. Diyaroglu et al. [19] demonstrate the applicability of peridynamics to accurately predict nonlinear transient deformation and damage behavior of composites under shock or blast types of loadings due to explosions. Hu and Madenci [20] present an application of peridynamics to predict damage initiation and growth in fiber-reinforced composites under cyclic loading. Jiang and Wang [21] extended the peridynamic laminate theory (PDLT) model by using a spherical horizon instead of adjacent-layer horizon and studied the open-hole tensile strength of composite laminate. Cuenca and Weckner et al. [22] investigated the application of peridynamics in dynamic fracture simulations for composite structures in high energy dynamic impact (HEDI) events. Baber et al. [23] used PD to model the low-velocity impact damage on composite laminates with z-pins. Zhou and Liu [24] studied the application of PD in analyzing the impact-induced delamination in laminated composite materials.

Open-hole tensile strength (OHT) of fiber-reinforced composite laminate is an important structural design allowable for composite aircraft. Analysis OHT results are as important as testing results due to overall consideration of cost and reliability for composite structure design. Reliable OHT prediction of fiber-reinforced composite laminate is a challenging problem [25, 26]. In the previous studies, PD gives impressive results in OHT prediction of fiber-reinforced composite laminates [15, 17, 27–29]. On the other hand, standard OHT test results also provide good benchmarks for validating PD composite models.

The present study is a further investigation of previously proposed PD composite model [21]. In the previous work, we extended the PDLT model [30, 31] by using a spherical horizon instead of adjacent-layer horizon and illustrated that transverse Poisson's effect can be taken into account. In the present study, energy-based failure criteria are introduced into the previous PD composite model. The energy-based failure criteria are derived following the approach proposed by Silling and Lehoucq [4]. Delamination fracture modes are distinguished in the present energy-based failure criteria. Three fiber-reinforced composite OHT testing results from published literatures are modeled by using the present PD composite model with energy-based failure criteria. The PD OHT predicted results are compared with testing results, and the PD OHT displacement field and damage modes are illustrated. The numerical analysis in the present study is carried out via GPU-parallel computing using PGI CUDA FORTRAN compiler.

2. Ordinary State-Based Peridynamic Model for Composite Laminates

2.1. Governing Equation. A three-dimensional PD composite model is proposed by Jiang and Wang [21] in the way of extending the PDLT model [30, 31] to spherical horizon. Transverse Poisson's ratio ν_{13} and ν_{23} can be considered in this PD composite model. The governing equation of this PD composite model is expressed as

$$\rho_{(k)}^{(n)} \ddot{\mathbf{u}}_{(k)}^{(n)} = \sum_{j=1}^{\infty} [\mathbf{t}_{(k)(j)} - \mathbf{t}_{(j)(k)}] \mathbf{V}_{(j)} + \mathbf{b}_{(k)}^{(n)}, \quad (1)$$

where $\rho_{(k)}^{(n)}$ is the density of material point $\mathbf{x}_{(k)}^{(n)}$, $\ddot{\mathbf{u}}_{(k)}^{(n)}$ is instantaneous acceleration of $\mathbf{x}_{(k)}^{(n)}$, and n denotes the layer number of laminates, as shown in Figure 1. $\mathbf{b}_{(k)}^{(n)}$ is the external load density. $\mathbf{t}_{(k)(j)}$ and $\mathbf{t}_{(j)(k)}$ are PD force density between $\mathbf{x}_{(k)}^{(n)}$ and $\mathbf{x}_{(j)}^{(n)}$, here $\mathbf{x}_{(j)}$ includes both in-plane material points and out-of-plane material points. The PD force density can be expressed as

$$\begin{aligned} \mathbf{t}_{(k)(j)} &= A_{(k)(j)} \frac{\mathbf{y}_{(j)} - \mathbf{y}_{(k)}^{(n)}}{|\mathbf{y}_{(j)} - \mathbf{y}_{(k)}^{(n)}|}, \\ \mathbf{t}_{(j)(k)} &= B_{(j)(k)} \frac{\mathbf{y}_{(k)}^{(n)} - \mathbf{y}_{(j)}}{|\mathbf{y}_{(k)}^{(n)} - \mathbf{y}_{(j)}|}, \end{aligned} \quad (2)$$

with

$$\begin{aligned} A_{(k)(j)} &= 2ad \frac{\delta}{|\mathbf{x}_{(j)} - \mathbf{x}_{(k)}^{(n)}|} \Lambda_{(k)(j)} \theta_{(k)} + 2\delta b s_{(k)(j)} \\ &\quad + 2\delta (\mu_F b_F + \mu_T b_T) s_{(k)(j)}^{(n(n))}, \\ B_{(j)(k)} &= 2ad \frac{\delta}{|\mathbf{x}_{(k)}^{(n)} - \mathbf{x}_{(j)}|} \Lambda_{(j)(k)} \theta_{(j)} + 2\delta b s_{(j)(k)} \\ &\quad + 2\delta (\mu_F b_F + \mu_T b_T) s_{(j)(k)}^{(n(n))}, \\ s_{(k)(j)} &= \frac{|\mathbf{y}_{(j)} - \mathbf{y}_{(k)}^{(n)}| - |\mathbf{x}_{(j)} - \mathbf{x}_{(k)}^{(n)}|}{|\mathbf{x}_{(j)} - \mathbf{x}_{(k)}^{(n)}|}, \\ s_{(k)(j)}^{(n(n))} &= \frac{|\mathbf{y}_{(j)}^{(n)} - \mathbf{y}_{(k)}^{(n)}| - |\mathbf{x}_{(j)}^{(n)} - \mathbf{x}_{(k)}^{(n)}|}{|\mathbf{x}_{(j)}^{(n)} - \mathbf{x}_{(k)}^{(n)}|}, \\ \mu_F &= \begin{cases} 1, & (\mathbf{x}_{(j)}^{(n)} - \mathbf{x}_{(k)}^{(n)}) \parallel \text{fiber direction}, \\ 0, & \text{otherwise}, \end{cases} \\ \mu_T &= \begin{cases} 1, & (\mathbf{x}_{(j)}^{(n)} - \mathbf{x}_{(k)}^{(n)}) \perp \text{fiber direction}, \\ 0 & \text{otherwise}, \end{cases} \end{aligned} \quad (3)$$

where $s_{(k)(j)}$ is the stretch of bonds, $s_{(k)(j)}^{(n(n))}$ denotes the in-plane fiber direction or in-plane transverse direction bond stretch, and δ is the radius of the horizon zone. The direction cosines of the relative position vectors between the material

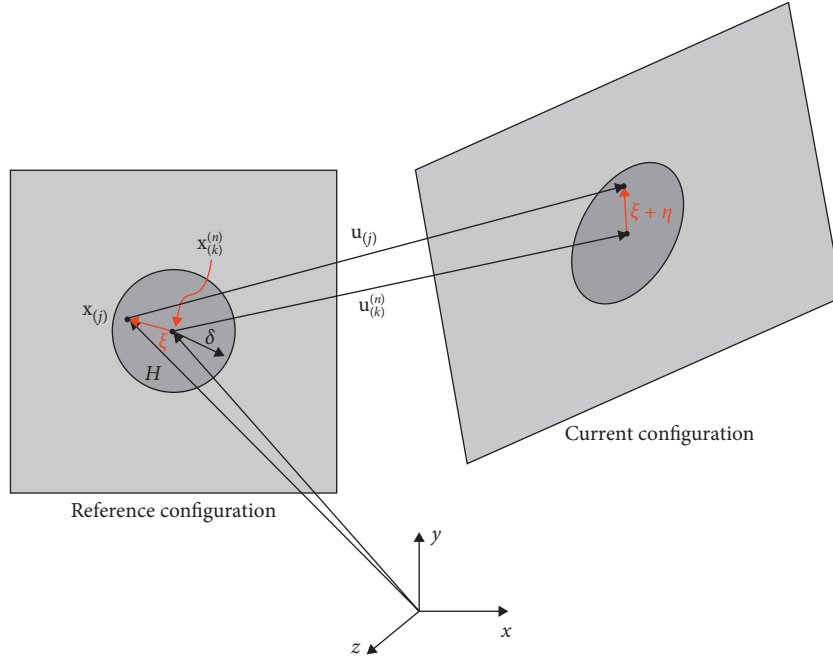


FIGURE 1: Peridynamic notations.

points $\mathbf{x}^{(k)}$ and $\mathbf{x}^{(j)}$ in the undeformed and deformed states are defined as

$$\Lambda_{(k)(j)} = \frac{\mathbf{y}^{(j)} - \mathbf{y}^{(k)}}{|\mathbf{y}^{(j)} - \mathbf{y}^{(k)}|} \cdot \frac{\mathbf{x}^{(j)} - \mathbf{x}^{(k)}}{|\mathbf{x}^{(j)} - \mathbf{x}^{(k)}|}. \quad (4)$$

The three-dimensional PD dilatation $\theta_{(k)}$ can be expressed as

$$\theta_{(k)} = d \sum_{j=1}^{\infty} \delta s_{(k)(j)} \Lambda_{(k)(j)} V_{(j)}. \quad (5)$$

The PD material parameters a and d characterize the effect of dilation and b , b_F , and b_T are associated with deformation of material points in arbitrary directions, in-plane fiber direction, and in-plane transverse direction, respectively. These parameters are related to material properties of composite laminates, horizon radius, and ply direction. The derivation procedures to get these PD material parameters can be found in [21].

$$\begin{aligned} a &= \frac{1}{2} (C_{33} - 3C_{55}), \\ d &= \frac{9}{4\pi\delta^4}, \\ b &= \frac{15C_{55}}{2\pi\delta^5}, \\ b_F &= \frac{C_{11} - C_{33}}{2\delta \sum_{j=1}^J |\mathbf{x}^{(j)} - \mathbf{x}^{(k)}| V_{(j)}^{(n)}}, \\ b_T &= \frac{C_{22} - C_{33}}{2\delta \sum_{j=1}^J |\mathbf{x}^{(j)} - \mathbf{x}^{(k)}| V_{(j)}^{(n)}}, \end{aligned} \quad (6)$$

where C_{11} , C_{22} , C_{33} , and C_{55} are coefficients of composite material stiffness matrix \mathbf{C} , and are defined as

$$\begin{aligned} C_{11} &= \frac{1 - \nu_{23}\nu_{32}}{E_2 E_3 \Delta}, \\ C_{22} &= \frac{1 - \nu_{13}\nu_{31}}{E_1 E_3 \Delta}, \\ C_{33} &= \frac{1 - \nu_{12}\nu_{21}}{E_1 E_2 \Delta}, \\ C_{55} &= G_{31}, \\ \Delta &= \frac{1 - \nu_{12}\nu_{21} - \nu_{23}\nu_{32} - \nu_{13}\nu_{31} - 2\nu_{21}\nu_{32}\nu_{13}}{E_1 E_2 E_3}. \end{aligned} \quad (7)$$

2.2. Energy-Based Failure Criteria. Following the approach for deriving the relationship between the critical bond breakage work and critical energy release rate by Silling and Lehoucq [4], energy-based failure criteria for delamination damage of fiber-reinforced composites are proposed.

This approach assumes that the energy consumed by a growing delamination front equals the work required, per unit delamination front area, to separate two halves of a body across a plane (Figure 2 for mode-I delamination). Suppose a plane A separates two halves of a three-dimensional body B into B_+ and B_- . The delamination front area a is on the plane. Consider a mode-I delamination motion with velocity field on Figure 2. The total energy E absorbed by P in this motion is

$$E = \int_0^t \mathcal{W}_{\text{abs}}(\mathcal{P}) dt' = \int_0^{t_0} \int_{\mathcal{P}} \int_{\mathcal{R}} t_z (v'_z - v_z) dV' dV dt. \quad (8)$$

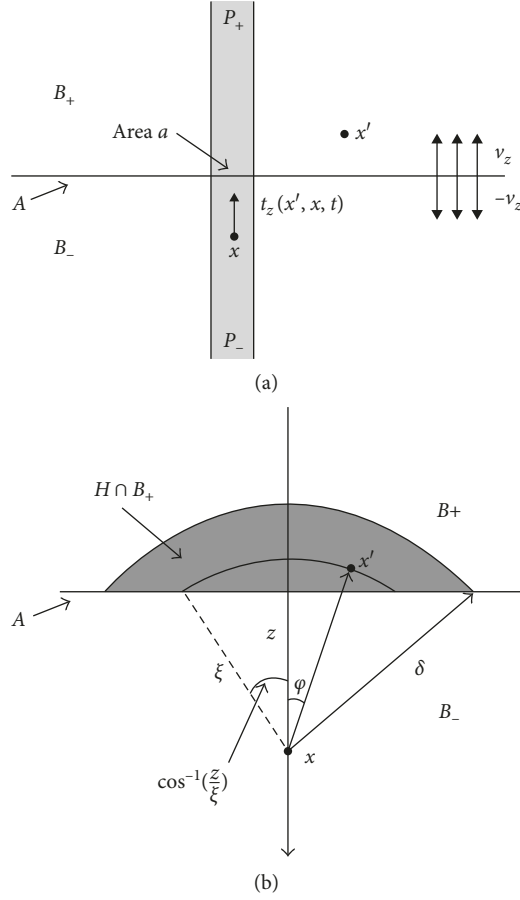


FIGURE 2: Surface energy by the total work absorbed by P_- separated from B_+ for mode-I delamination [4].

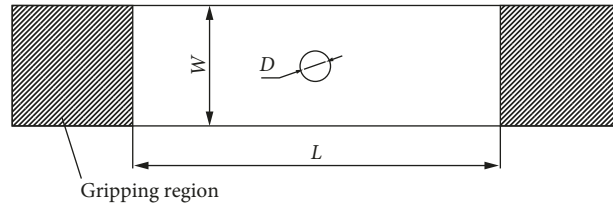


FIGURE 3: Schematic of open-hole tensile test specimen.

The assumed critical bond breakage work w_{IC} in this motion is

$$\int_0^{t_0} t_z (v'_z - v_z) dt = w_{IC}. \quad (9)$$

Therefore,

$$\begin{aligned} E &= w_{IC} \int_{\mathcal{P}} \int_{\mathcal{B}} dV' dV = 2w_{IC} \int_{\mathcal{P}_-} \int_{\mathcal{B}_+} dV' dV \\ &= 2w_{IC} a \int_0^{2\pi} \int_0^{\delta} \int_z^{\delta} \int_0^{\cos^{-1}(z/\xi)} \xi^2 \sin \varphi d\varphi d\xi dz d\theta \quad (10) \\ &= \frac{\pi w_{IC} \delta^4 a}{2}. \end{aligned}$$

When the critical energy release rate is reached,

$$G_{IC} = \frac{E}{a} = \frac{\pi w_{IC} \delta^4 a}{2a} = \frac{1}{2} \pi w_{IC} \delta^4. \quad (11)$$

$$w_{IC} = \frac{2G_{IC}}{\pi \delta^4}.$$

Similarly, we can get the critical bond breakage work for mode-II and mode-III delamination as

$$w_{IIC} = \frac{2G_{IIC}}{\pi \delta^4}, \quad (12)$$

$$w_{IIIC} = \frac{2G_{IIIC}}{\pi \delta^4}.$$

From the above derivation, energy-based failure criteria for delamination damage are proposed,

TABLE 1: Specimen configuration of composite laminates with open-hole.

Specimen	Material system	L	W	D	Thickness	Layup	h (ply)
OHT1 [25]	IM7/8552	64	16	3.175	1	[90/45/0/-45] _S	0.125
OHT2 [17]	IM-7/977-3	138.43	38.1	6.35	2	[0/45/90/-45] _{2S}	0.125
OHT3 [34]	IM7/8552	100	36	6	3.144	[90/0/45/-45] _{3S}	0.131

Unit: mm.

$$\left\{ \begin{array}{l} \left| \frac{w_I}{w_{IC}} \right| \geq 1, \quad w_I = \int_0^{t_0} t_z (v'_z - v_z) dt = t_z (u'_z - u_z), \\ \text{for mode-I delamination,} \\ \left| \frac{w_{II}}{w_{IIC}} \right| \geq 1, \quad w_{II} = \int_0^{t_0} t_x (v'_x - v_x) dt = t_x (u'_x - u_x), \\ \text{for mode-II delamination,} \\ \left| \frac{w_{III}}{w_{IIIC}} \right| \geq 1, \quad w_{III} = \int_0^{t_0} t_y (v'_y - v_y) dt = t_y (u'_y - u_y), \\ \text{for mode-III delamination.} \end{array} \right. \quad (13)$$

Intralayer failure criteria used in the present study is similar to other PD models [15, 17]. When the bond stretch between two material points exceeds a critical value, the interaction between these two material points is irreversibly removed. The critical stretches for the fiber bonds and matrix bonds can be calculated by

$$\left\{ \begin{array}{l} s_0^{\text{ft}} = \frac{X^T}{E_1}, \quad s \geq 0 \quad \text{fiber bonds,} \\ s_0^{\text{fc}} = \frac{X^C}{E_1}, \quad s < 0 \quad \text{fiber bonds,} \\ s_0^{\text{mt}} = \frac{Y^T}{E_2}, \quad s \geq 0 \quad \text{fiber bonds,} \\ s_0^{\text{mc}} = \frac{Y^C}{E_2}, \quad s < 0 \quad \text{matrix bonds,} \end{array} \right. \quad (14)$$

where X^T , X^C , Y^T , and Y^C are strengths of composite materials.

Local damage at a material point is defined as the weighted ratio of the number of eliminated interactions to the total number of initial interactions of the material point with its family members. The local damage at a point can be quantified as [3, 19]

$$\varphi(\mathbf{x}, t) = 1 - \frac{\int_H \mu(x' - \mathbf{x}, t) dV'}{\int_H dV'}. \quad (15)$$

The status variable, μ , is defined as

$$\mu = \begin{cases} 1, & \text{no damage,} \\ 0, & \text{damage.} \end{cases} \quad (16)$$

Using the failure criteria presented above, three kinds of typical damage modes of composite laminates can be captured: fiber breakage, matrix cracking, and delamination. These damage modes are indicated by

TABLE 2: Intralayer material properties of IM-7/977-3 [17] ($\rho = 1603 \text{ kg/m}^3$).

E_1 (GPa)	E_2 (GPa)	G_{12} (GPa)	ν_{12}	X^T (MPa)	X^C (MPa)	Y^T (MPa)	Y^C (MPa)
164.3	8.977	5.02	0.32	2905	1680	100	247

TABLE 3: Interlayer material properties of IM-7/977-3 [17].

G_{IC} (MPa)	G_{IIC} (MPa)	G_{IIIC} (MPa)
0.256	0.6499	0.6499

TABLE 4: Intralayer material properties of IM7/8552 [26, 34].

E_1 (GPa)	E_2 (GPa)	G_{12} (GPa)	ν_{12}	X^T (MPa)	X^C (MPa)	Y^T (MPa)	Y^C (MPa)
161	11.38	5.17	0.32	2905	1680	100	247

TABLE 5: Interlayer material properties of IM7/8552 [34].

G_{IC} (MPa)	G_{IIC} (MPa)	G_{IIIC} (MPa)
0.2774	0.7879	0.7879

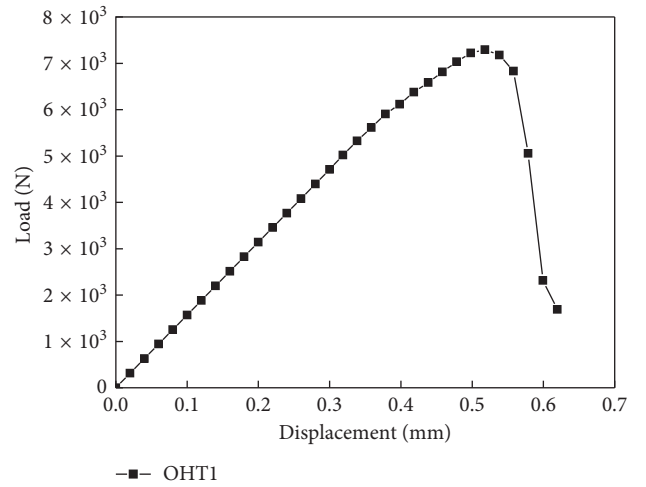


FIGURE 4: PD predicted load-displacement for OHT1.

TABLE 6: Open-hole tensile strength prediction of fiber-reinforced composite laminates.

Specimen	Experiment (MPa)	PD (MPa)	Relative error
OHT1	481	456.04	-5.19%
OHT2	554	564.1	1.82%
OHT3	438.7	455.89	3.92%

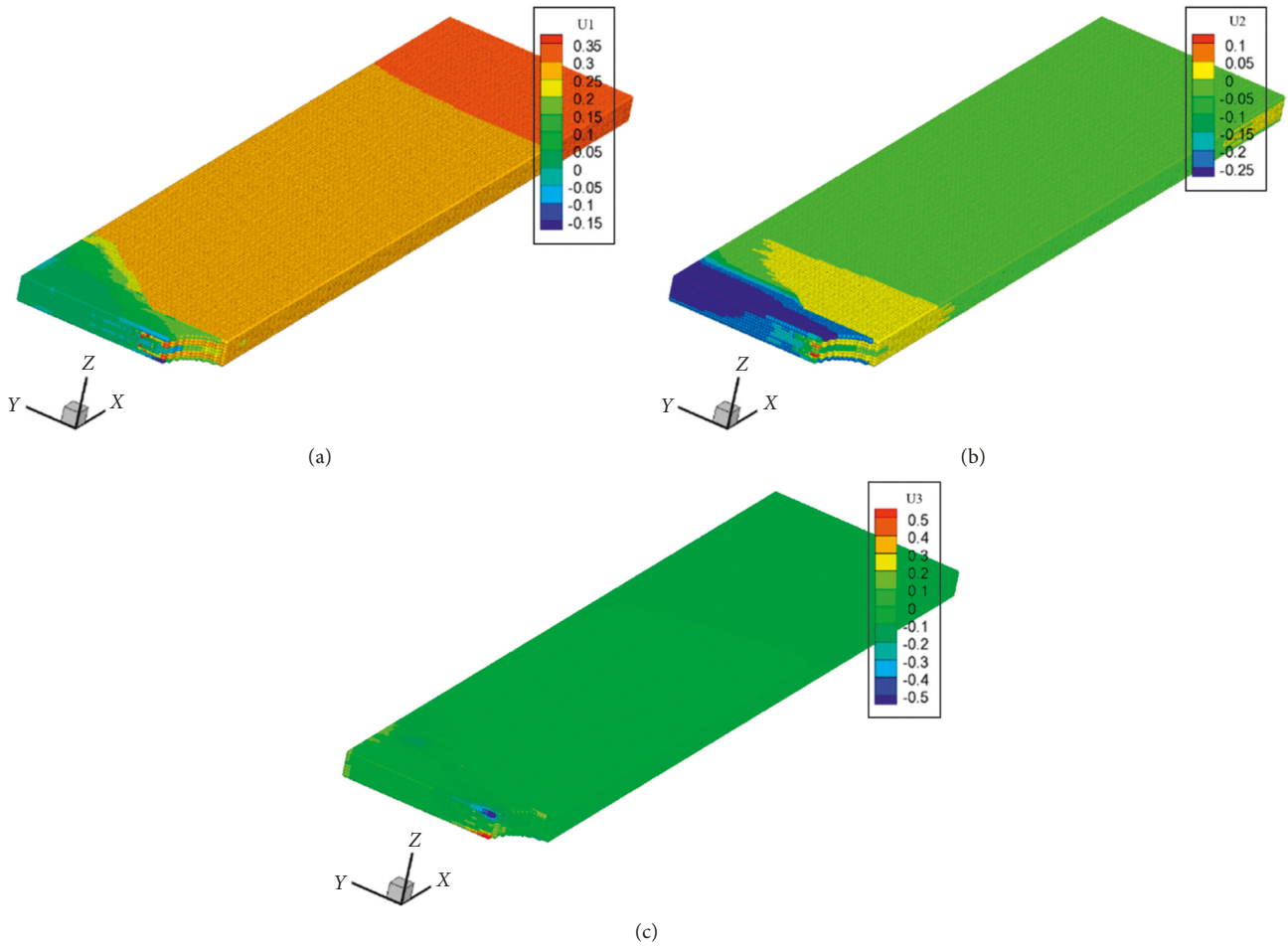


FIGURE 5: PD predicted displacement field for OHT1.

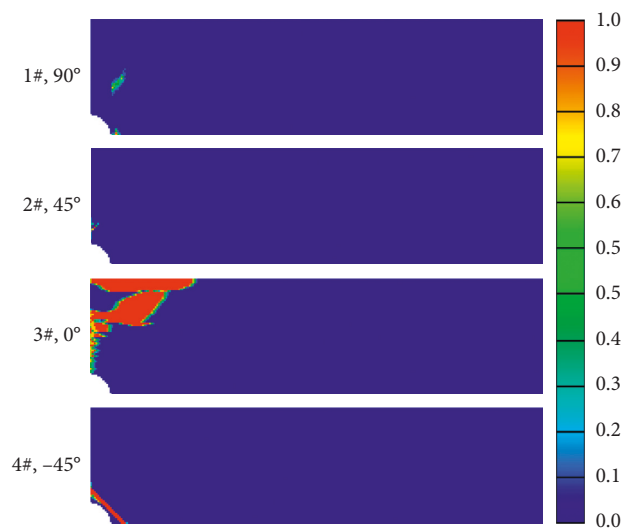


FIGURE 6: Fiber breakage for each layer of OHT1.

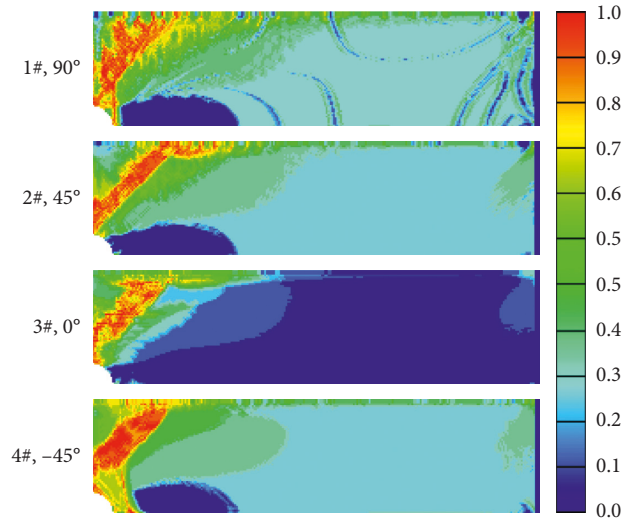


FIGURE 7: Matrix crack for each layer of OHT1.

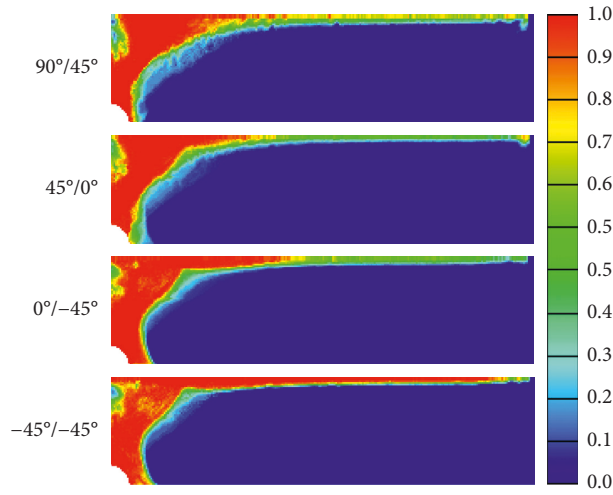


FIGURE 8: Delamination between each layer of OHT1.

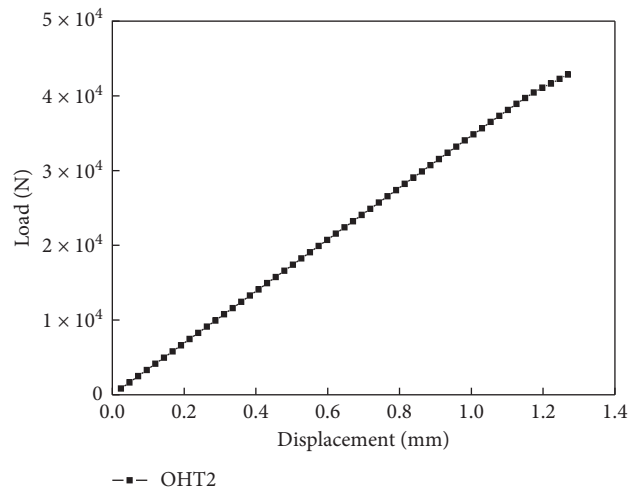


FIGURE 9: PD predicted load-displacement for OHT2.

TABLE 7: Comparison of predicted open-hole tensile strength of OHT2 with other peridynamic models (MPa).

Exp.	PDLT [28]	Bond-based PD [17]	Current model
554	528.42 (-4.62%)	541.624 (-2.23%)	564.1 (1.82%)

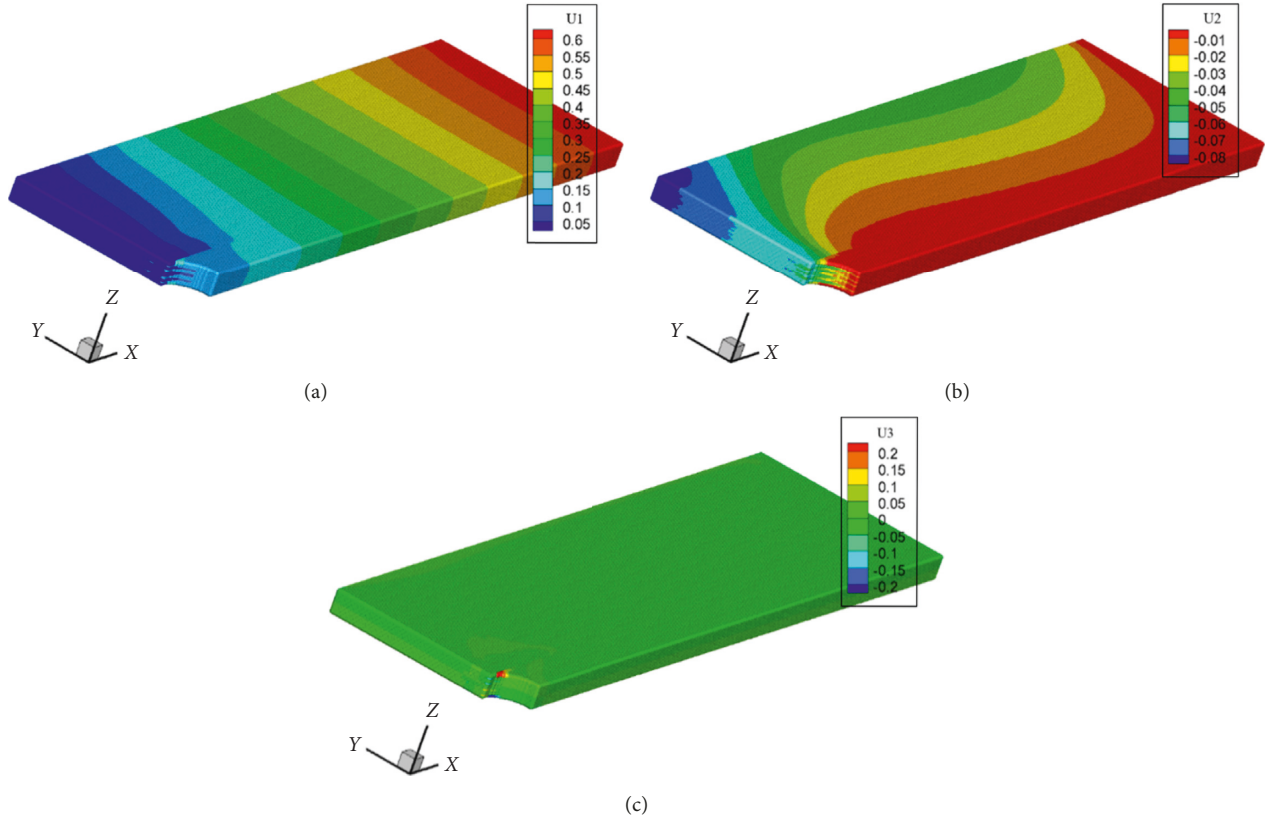


FIGURE 10: PD predicted displacement field for OHT2.

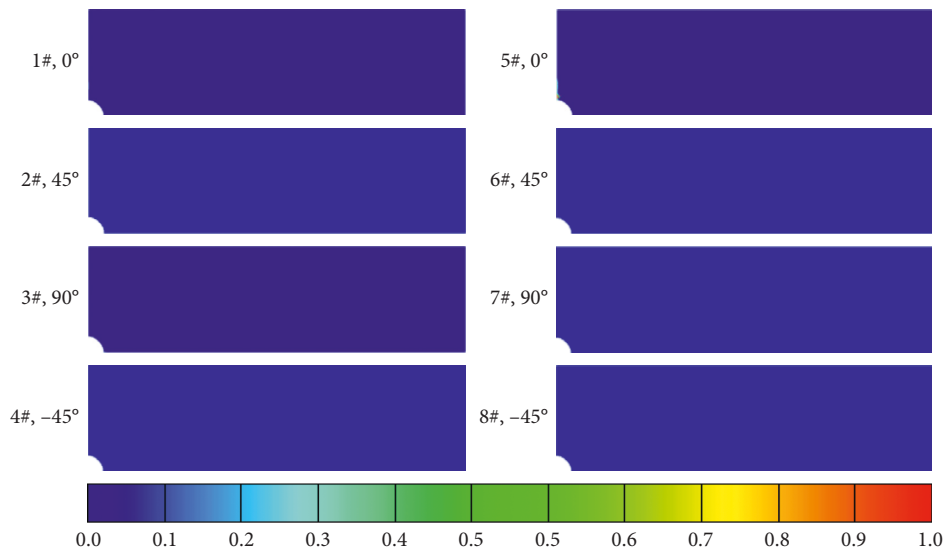


FIGURE 11: Fiber breakage for each layer of OHT2.

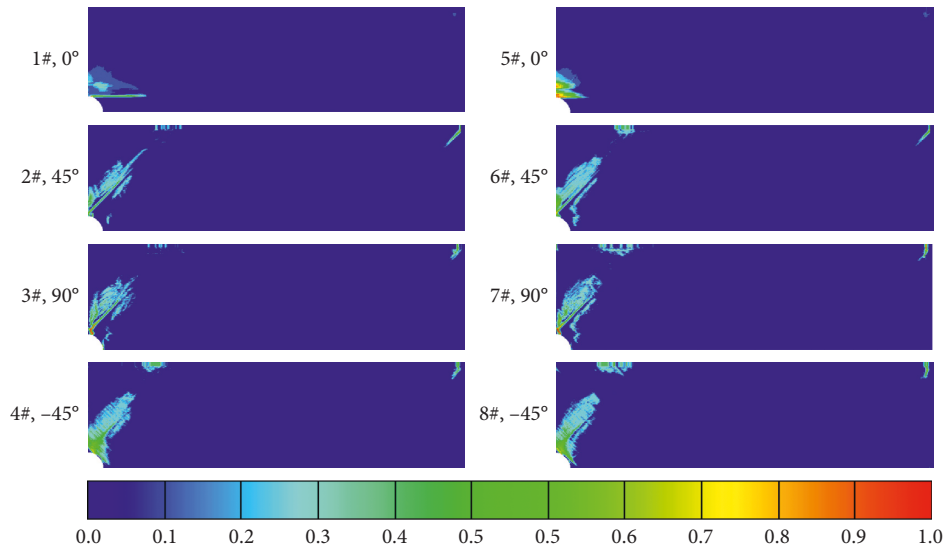


FIGURE 12: Matrix crack for each layer of OHT2.

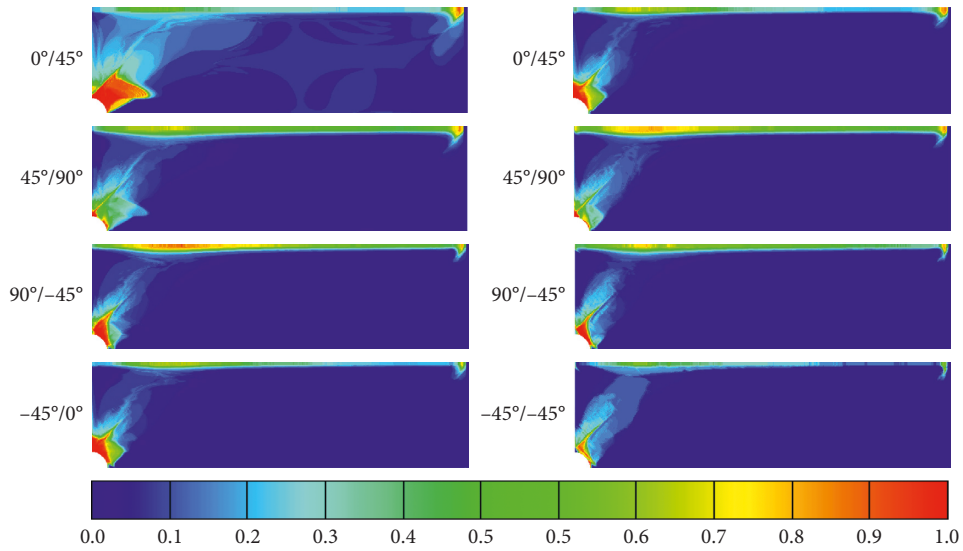


FIGURE 13: Delamination between each layer of OHT2.

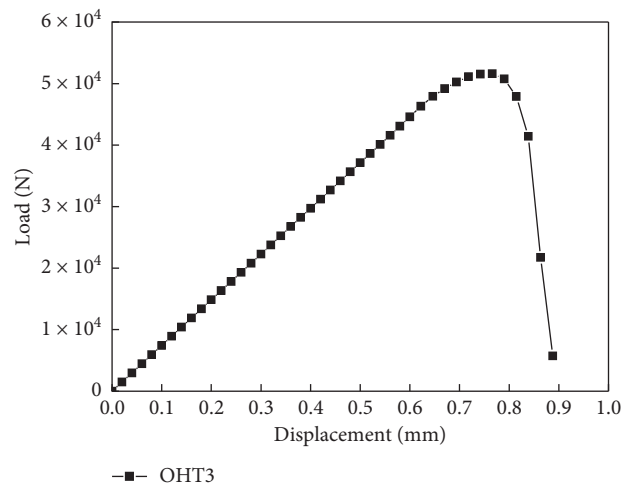


FIGURE 14: PD predicted load-displacement for OHT3.

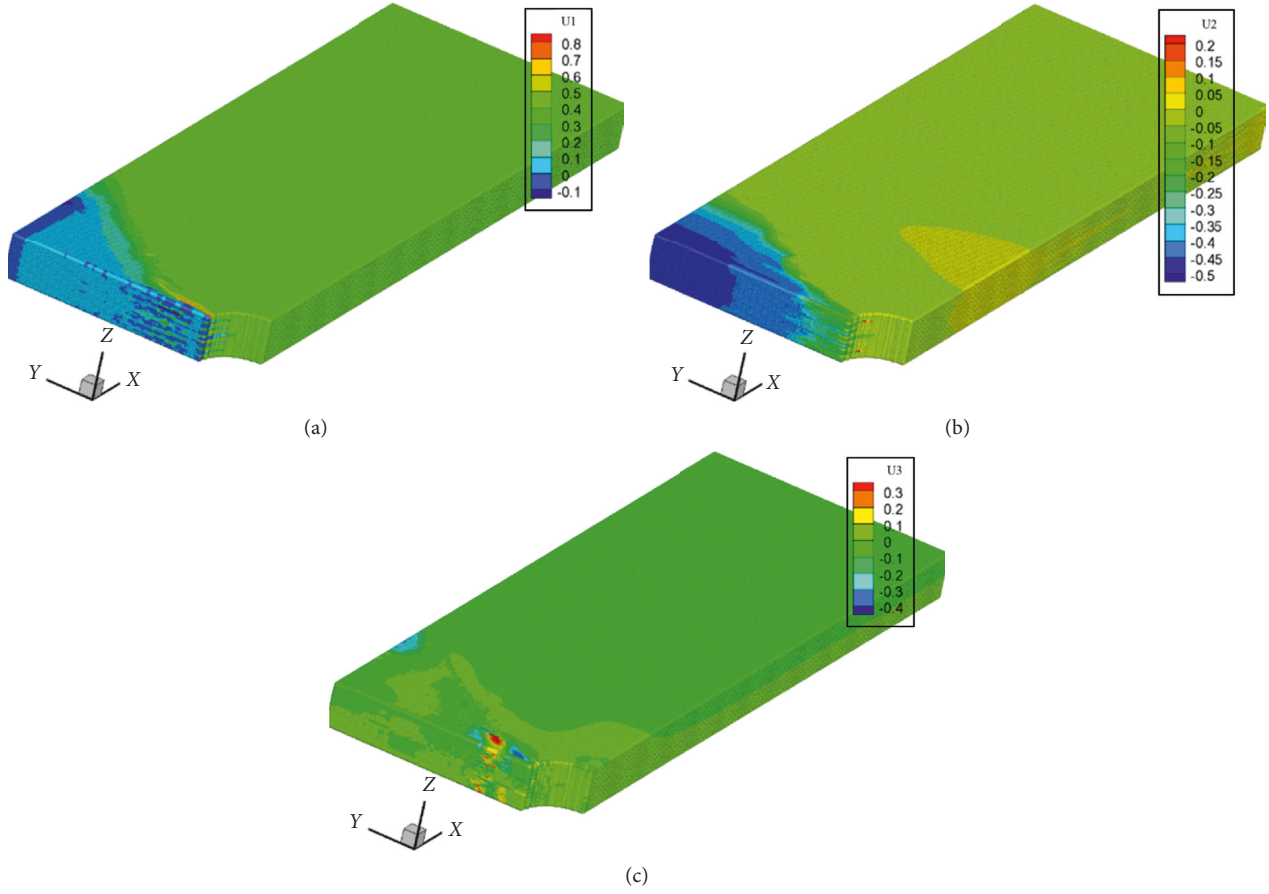


FIGURE 15: PD predicted displacement field for OHT3.

$$\left\{ \begin{array}{l}
 \varphi_{\text{fiber breakage}} = 1 - \frac{\sum_{j=1}^J \mu_{(k)(j)}^{(n)}}{J}, \\
 \varphi_{\text{matrix cracking}} = 1 - \frac{\sum_{j=1}^{N_{(k)}^{(n)}} \mu_{(k)(j)}^{(n)}}{N_{(k)}^{(n)}}, \\
 \varphi_{\text{out-of-plane_upper}}^{(n)} = 1 - \frac{\sum_{j=1}^{N_{(k)}^{(\text{upper})}} \mu_{(k)(j)}^{(n)}}{N_{(k)}^{(\text{upper})}}, \\
 \varphi_{\text{out-of-plane_lower}}^{(n+1)} = 1 - \frac{\sum_{j=1}^{N_{(k)}^{(\text{lower})}} \mu_{(k)(j)}^{(n)}}{N_{(k)}^{(\text{lower})}}, \\
 \varphi_{\text{delamination}}^{(n+1)} = \frac{1}{2} \left(\varphi_{\text{out-of-plane_upper}}^{(n)} + \varphi_{\text{out-of-plane_lower}}^{(n+1)} \right),
 \end{array} \right. \quad (17)$$

where J is the number of fiber material points inside the horizon, $N_{(k)}^{(n)}$ is the number of matrix material points inside the horizon, $N_{(k)}^{(\text{upper})}$ is the number of upper side interlayer material points inside the horizon, and $N_{(k)}^{(\text{lower})}$ is the number of lower side interlayer material points inside the horizon.

3. Numerical Implementation

Although the peridynamic governing equation is in dynamic form, it can still be used to solve quasi-static or static problems by using the adaptive dynamic relaxation (ADR) method [32].

According to the ADR method, equation (1) at the n th iteration can be rewritten:

$$\ddot{\mathbf{U}}^n(\mathbf{X}, t^n) + c^n \dot{\mathbf{U}}^n(\mathbf{X}, t^n) = \mathbf{D}^{-1} \mathbf{F}^n(\mathbf{U}^n, \mathbf{U}^n, \mathbf{X}, \mathbf{X}'), \quad (18)$$

where \mathbf{D} is the fictitious diagonal density matrix and c is the damping coefficient which can be expressed by

$$c^n = 2 \sqrt{\frac{((\mathbf{U}^n)^T \mathbf{1} \mathbf{K}^n \mathbf{U}^n)}{((\mathbf{U}^n)^T \mathbf{U}^n)}}, \quad (19)$$

in which $\mathbf{1} \mathbf{K}^n$ is the diagonal "local" stiffness matrix, which is given as

$${}^1 K_{ii}^n = -\frac{(F_i^n / \lambda_{ii} - F_i^{n-1} / \lambda_{ii})}{\Delta t \dot{u}_i^{n-1/2}}, \quad (20)$$

where F_i^n is the value of force vector \mathbf{F}^n at material point \mathbf{x} , which includes both the peridynamic force state vector and external forces, and λ_{ii} is the diagonal elements of \mathbf{D} which should be large enough to avoid numerical divergence.

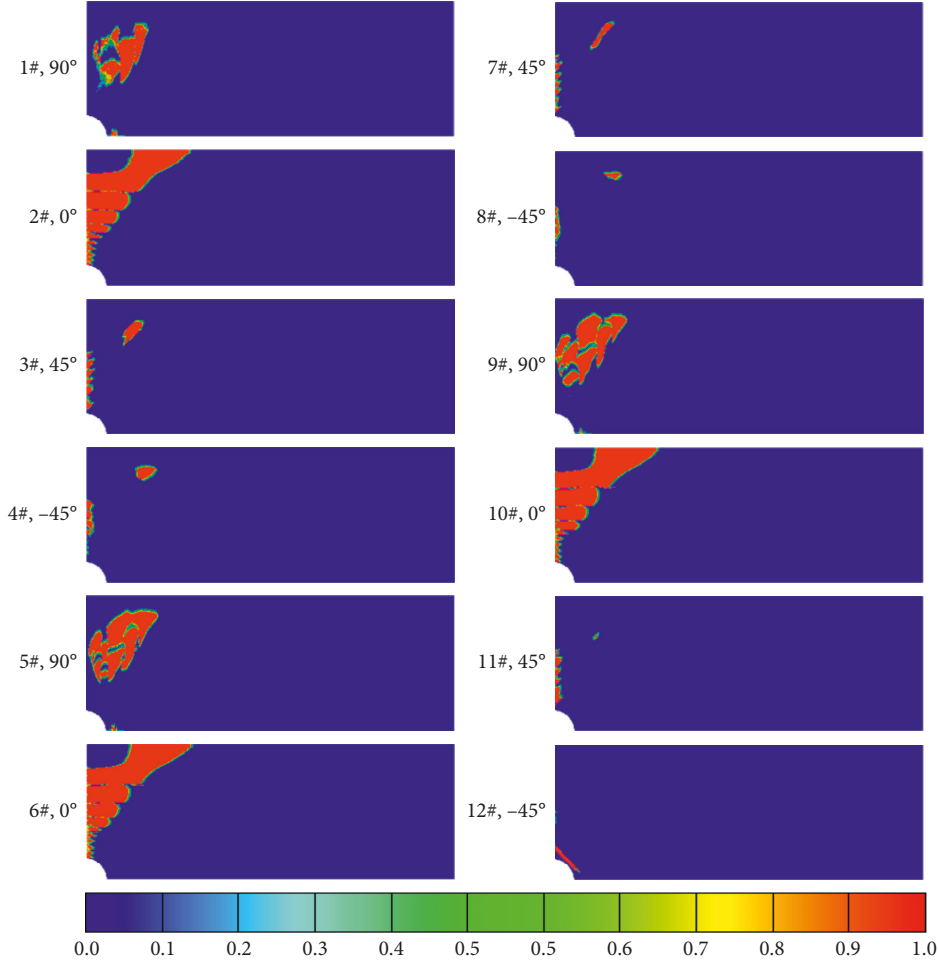


FIGURE 16: Fiber breakage for each layer of OHT3.

By utilizing central-difference explicit integration, displacements, and velocities for the next time step can be obtained:

$$\dot{\mathbf{U}}^{n+1/2} = \frac{\left((2 - c^n \Delta t) \dot{\mathbf{U}}^{n-1/2} + 2\Delta t \mathbf{D}^{-1} \mathbf{F}^n \right)}{(2 + c^n \Delta t)}, \quad (21)$$

$$\dot{\mathbf{U}}^{n+1} = \mathbf{U}^n + \Delta t \dot{\mathbf{U}}^{n+1/2}.$$

To start the iteration process, we assume that $\mathbf{U}^0 \neq 0$ and $\dot{\mathbf{U}}^0 = 0$, so the integration can be started by the following equation:

$$\dot{\mathbf{U}}^{1/2} = \frac{\Delta t \mathbf{D}^{-1} \mathbf{F}^0}{2}. \quad (22)$$

Due to the large computational amount of PD model, GPU-parallel computing is introduced. The PGI CUDA FORTRAN compiler, PGI/17.10 Community Edition, is used for compiling. The GPU node at Cranfield University Delta HPC Cluster is applied for running the GPU-parallel program. The GPU block threads are fixed to 256, and the number of blocks is depending on the total number of parallel processes [33].

4. Numerical Results

4.1. Summary of the Testing Specimens. The schematic of open-hole tensile test specimen is shown in Figure 3. Three OHT testing specimens are chosen from the published literatures and renumbered as OHT1, OHT2, and OHT3 as shown in Table 1. The material system, dimensions, and layup of these specimens are also listed in Table 1. The intralayer and interlayer material properties of each material system are shown in Tables 2–5.

4.2. OHT1 [90/45/0/-45]_S. Due to the large computational cost of PD, the quarter (1/4) model is used for modeling. The 1/4 model mesh size for OHT1 is $254 \times 64 \times 8$. The PD predicted load-displacement for the test is shown in Figure 4. The experimental and PD predicted strength is shown in Table 6. As we can see, the relative error of PD predicted strength for OHT1 is -5.19% . The PD predicted displacement field is shown in Figure 5. The fracture surface is very clearly detected from displacement field U_1 , which is relatively hard to see in FEM. Three typical damage patterns: fiber breakage, matrix crack for each layer, and delamination between each layer of

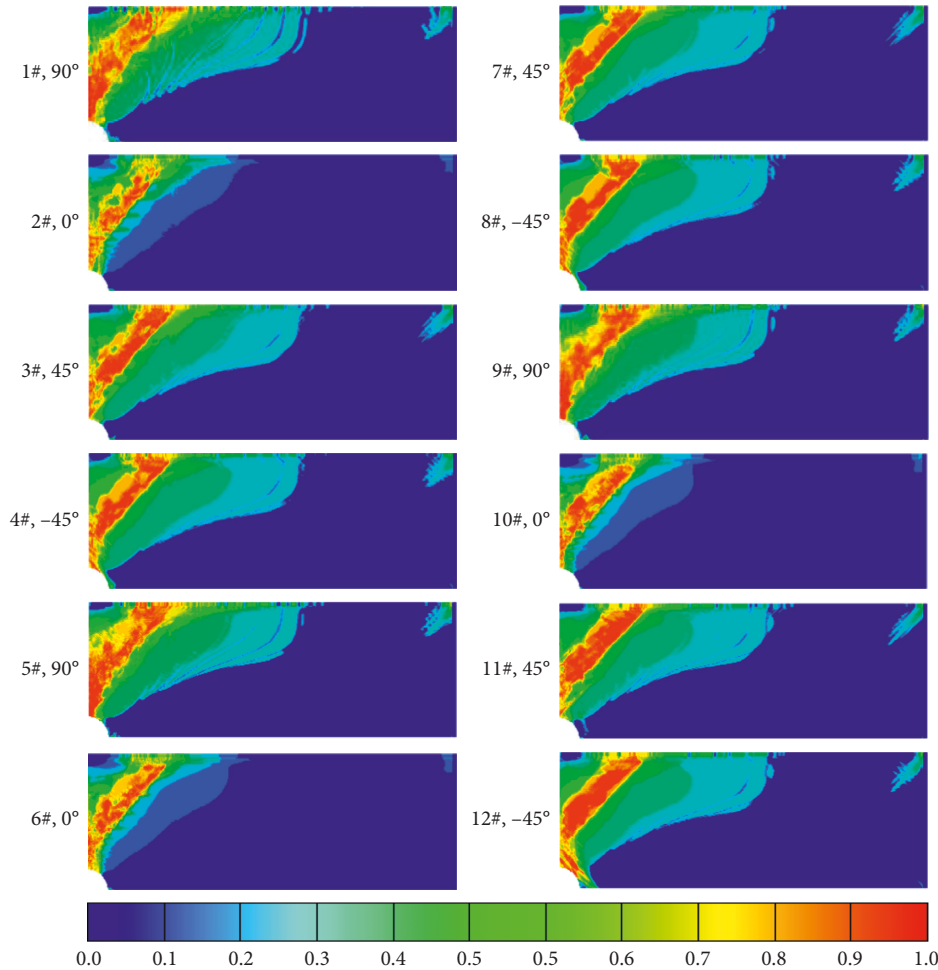


FIGURE 17: Matrix crack for each layer of OHT3.

OHT1, are shown in Figures 6–8. It can be seen that the most obvious fiber breakage is in 0° plies, and the interaction of the three damage modes leads to the final failure of the specimen.

4.3. *OHT2* $[0/45/90/-45]_{2S}$. The 1/4 model mesh size for OHT2 is $554 \times 152 \times 16$. The PD predicted load-displacement for the test is shown in Figure 9. The experimental and PD predicted strength is shown in Table 6. As we can see, the relative error of PD predicted strength for OHT2 is 1.82%. Table 7 compares the current model's result with other Peridynamic-based results. It can be seen that these three Peridynamic models all have good accuracy in predicting open-hole tensile strength of OHT2, and the model proposed in the present study gives better result than previous models.

The PD predicted displacement field is shown in Figure 10. The fracture surface is along the hole edge in x direction. Three typical damage patterns, fiber breakage, matrix crack for each layer, and delamination between each layer of OHT2 are shown in Figures 11–13. It can be seen that fiber breakage is very few for OHT2, only happens around the hole edge of ply-5# (0°). The final failure of OHT2 happens mainly due to matrix crack and delamination.

4.4. *OHT3* $[90/0/45/-45]_{3S}$. The 1/4 model mesh size for OHT3 is $382 \times 138 \times 24$. The PD predicted load-displacement for the test is shown in Figure 14. The experimental and PD predicted strength is shown in Table 6. As we can see, the relative error of PD predicted strength for OHT3 is 3.92%. The PD predicted displacement field is shown in Figure 15. The fracture surface is also very clearly detected from displacement field U1. Three typical damage patterns, fiber breakage, matrix crack for each layer, and delamination between each layer of OHT3, are shown in Figures 16–18. It can be seen that fiber breakage also happens mainly in 0° plies as OHT1, and the interaction of the three damage modes leads to the final failure of the specimen.

5. Discussion

It can conclude from the numerical results in Sections 4.2–4.4 that the current PD composite model with energy-based failure criteria can accurately predict the open-hole tensile strength of fiber-reinforced composite laminate. The fracture surface can be clearly detected by displacement field in loading direction. Three typical damage modes of fiber-reinforced composite laminate: fiber breakage, matrix crack, and delamination can also be captured.

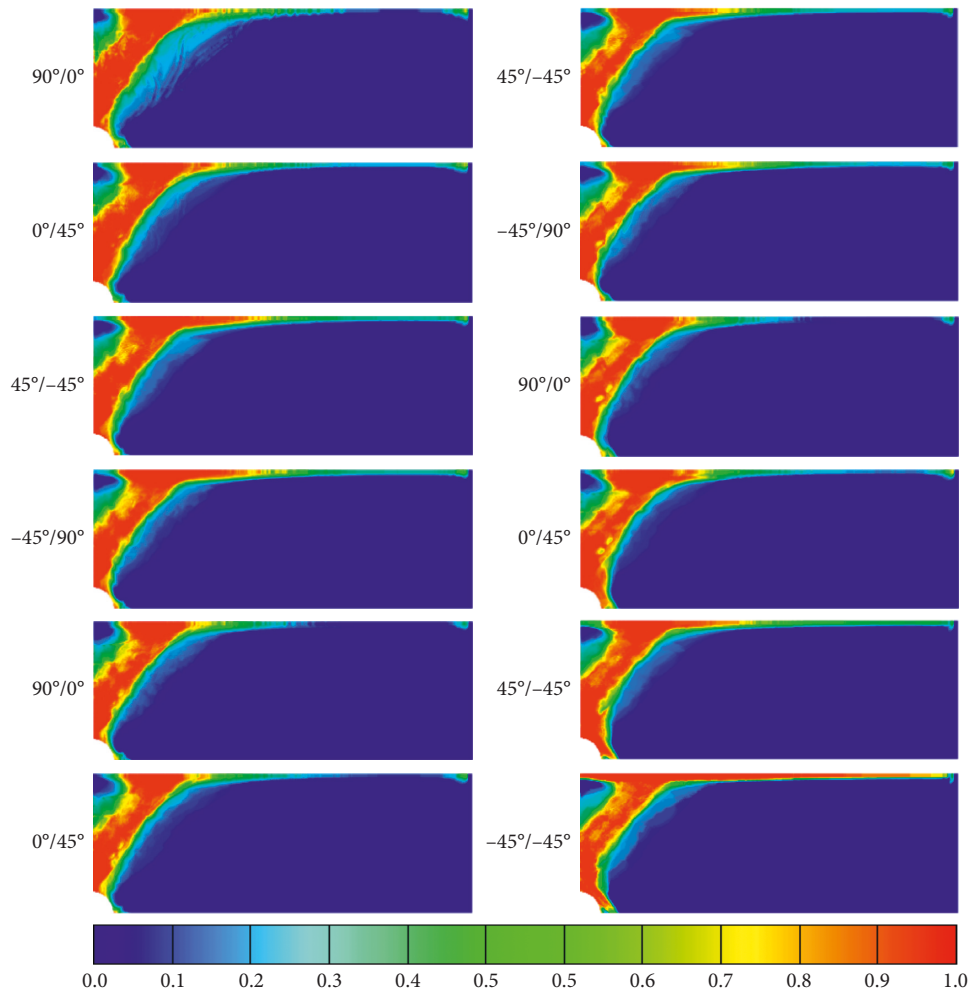


FIGURE 18: Delamination between each layer of OHT3.

6. Conclusion

Open-hole tensile (OHT) strength prediction of fiber-reinforced composite laminate is an important and challenging problem. Peridynamics (PD) is proved to have advantages in dealing with fracture and damage of composite. In the present study, we further investigated the previously proposed PD composite model by introducing energy-based failure criteria. Different fracture modes for delamination damage can be distinguished in these energy-based failure criteria. Three OHT testing results of fiber-reinforced composite laminate are chosen from the literature and modeled by the present PD composite model with energy-based failure criteria. It is shown that the present PD composite model with energy-based failure criteria can accurately predict the OHT strength of fiber-reinforced composite laminate. The fracture surface can be clearly detected. The typical failure modes of composite, fiber breakage, matrix crack, and delamination, are also illustrated in detail for the three testing specimens. The numerical results in the present study validate the accuracy and reliability of the current PD composite model with energy-based failure criteria.

Data Availability

Previously reported (experimental) data were used to support this study and are available at <http://10.1016/j.compstruct.2016.05.063>; <http://10.1007/s10704-009-9333-8>; and <http://10.1016/j.compscitech.2007.02.005>. These prior studies (and datasets) are cited at relevant places within the text as references [17, 25, 34].

Conflicts of Interest

The authors declare that they have no conflicts of interest.

Acknowledgments

The authors acknowledge the financial support from the China Scholarship Council (CSC No. 201706230169).

References

- [1] F. Bobaru, J. T. Foster, P. H. Geubelle, and S. A. Silling, *Handbook of Peridynamic Modeling*, Chapman and Hall/CRC, New York, NY, USA, 1st edition, 2016.

- [2] S. A. Silling, "Reformulation of elasticity theory for discontinuities and long-range forces," *Journal of the Mechanics and Physics of Solids*, vol. 48, no. 1, pp. 175–209, 2000.
- [3] S. A. Silling and E. Askari, "A meshfree method based on the peridynamic model of solid mechanics," *Computers and Structures*, vol. 83, no. 17–18, pp. 1526–1535, 2005.
- [4] S. A. Silling and R. B. Lehoucq, *Peridynamic Theory of Solid Mechanics*, ELSEVIER, Vol. 44, ELSEVIER, Amsterdam, Netherlands, 2010.
- [5] E. Askari, J. Xu, and S. Silling, "Peridynamic analysis of damage and failure in composites," in *Proceedings of 44th AIAA Aerospace Sciences Meeting and Exhibit*, pp. 1–12, Reno, NV, USA, January 2006.
- [6] J. F. Xu, A. Askari, O. Weckner, H. Razi, and S. Silling, "Damage and failure analysis of composite laminates under biaxial loads," in *Proceedings of 48th AIAA/ASME/ASCE/AHS/ASC Structures, Structural Dynamics, and Materials Conference*, Honolulu, HI, USA, April 2007.
- [7] J. Xu, A. Askari, O. Weckner, and S. Silling, "Peridynamic analysis of impact damage in composite laminates," *Journal of Aerospace Engineering*, vol. 21, no. 3, pp. 187–194, 2008.
- [8] B. Kilic, A. Agwai, and E. Madenci, "Peridynamic theory for progressive damage prediction in center-cracked composite laminates," *Composite Structures*, vol. 90, no. 2, pp. 141–151, 2009.
- [9] E. Oterkus, A. Barut, and E. Madenci, "Damage growth prediction from loaded composite fastener holes by using peridynamic theory," in *Proceedings of 51st AIAA/ASME/ASCE/AHS/ASC Structures, Structural Dynamics, and Materials Conference*, Orlando, FL, USA, April 2010.
- [10] W. Hu, Y. D. Ha, and F. Bobaru, "Modeling dynamic fracture and damage in a fiber-reinforced composite lamina with peridynamics," *International Journal for Multiscale Computational Engineering*, vol. 9, no. 6, pp. 707–726, 2011.
- [11] W. Hu, Y. D. Ha, and F. Bobaru, "Peridynamic model for dynamic fracture in unidirectional fiber-reinforced composites," *Computer Methods in Applied Mechanics and Engineering*, vol. 217–220, pp. 247–261, 2012.
- [12] E. Oterkus and E. Madenci, "Peridynamic theory for damage initiation and growth in composite laminate," *Key Engineering Materials*, vol. 488–489, pp. 355–358, 2012.
- [13] E. Oterkus and E. Madenci, "Peridynamic analysis of fiber-reinforced composite materials," *Journal of Mechanics of Materials and Structures*, vol. 7, no. 1, pp. 45–84, 2012.
- [14] E. Oterkus, E. Madenci, O. Weckner, S. Silling, P. Bogert, and A. Tessler, "Combined finite element and peridynamic analyses for predicting failure in a stiffened composite curved panel with a central slot," *Composite Structures*, vol. 94, no. 3, pp. 839–850, 2012.
- [15] Y. L. Hu, Y. Yu, and H. Wang, "Peridynamic analytical method for progressive damage in notched composite laminates," *Composite Structures*, vol. 108, no. 1, pp. 801–810, 2014.
- [16] Y. L. Hu, N. V. De Carvalho, and E. Madenci, "Peridynamic modeling of delamination growth in composite laminates," *Composite Structures*, vol. 132, pp. 610–620, 2015.
- [17] Y. L. Hu and E. Madenci, "Bond-based peridynamic modeling of composite laminates with arbitrary fiber orientation and stacking sequence," *Composite Structures*, vol. 153, pp. 139–175, 2016.
- [18] C. Sun and Z. Huang, "Peridynamic simulation to impacting damage in composite laminate," *Composite Structures*, vol. 138, pp. 335–341, 2016.
- [19] C. Diyaroglu, E. Oterkus, E. Madenci, T. Rabczuk, and A. Siddiq, "Peridynamic modeling of composite laminates under explosive loading," *Composite Structures*, vol. 144, pp. 14–23, 2016.
- [20] Y. L. Hu and E. Madenci, "Peridynamics for fatigue life and residual strength prediction of composite laminates," *Composite Structures*, vol. 160, pp. 169–184, 2017.
- [21] X. W. Jiang and H. Wang, "Ordinary state-based peridynamics for open-hole tensile strength prediction of fiber-reinforced composite laminates," *Journal of Mechanics of Materials and Structures*, vol. 13, no. 1, pp. 53–82, 2018.
- [22] O. Weckner, F. Cuenca, S. Silling, M. Rassaian, and J. Pang, "Determination of ballistic limit for IM7/8552 using peridynamics," in *Proceedings of 2018 AIAA/ASCE/AHS/ASC Structures, Structural Dynamics, and Materials Conference*, Kissimmee, FL, USA, January 2018.
- [23] F. Baber, V. Ranatunga, and I. Guven, "Peridynamic modeling of low-velocity impact damage in laminated composites reinforced with z-pins," *Journal of Composite Materials*, vol. 52, no. 25, pp. 3491–3508, 2018.
- [24] W. Zhou and D. Liu, "Analyzing impact induced delamination in laminated composite materials with peridynamic modeling," in *Proceedings of AIAA/ASCE/AHS/ASC Structures, Structural Dynamics, and Materials Conference*, Reston, VA, USA, January 2018.
- [25] S. R. Hallett, B. G. Green, W. G. Jiang, K. H. Cheung, and M. R. Wisnom, "The open hole tensile test: a challenge for virtual testing of composites," *International Journal of Fracture*, vol. 158, no. 2, pp. 169–181, 2009.
- [26] S. Hallett, W. G. Jiang, and M. Wisnom, "The effect of stacking sequence on thickness scaling of tests on open hole tensile composite specimens," in *Proceedings of 48th AIAA/ASME/ASCE/AHS/ASC Structures, Structural Dynamics, and Materials Conference*, Honolulu, HI, USA, April 2007.
- [27] Y. Yu, S. S. Liu, S. L. Zhao, and Z. Yu, "The nonlinear inplane behavior and progressive damage modeling for laminate by peridynamics," in *Proceedings of ASME 2016 International Mechanical Engineering Congress and Exposition*, Phoenix, AZ, USA, November 2016.
- [28] Y. Hu, E. Madenci, and N. D. Phan, "Peridynamics for predicting tensile and compressive strength of notched composites," in *Proceedings of 57th AIAA/ASCE/AHS/ASC Structures, Structural Dynamics, and Materials Conference*, San Diego, CA, USA, January 2016.
- [29] K. Colavito, A. Barut, E. Madenci, and N. Phan, "Residual strength of composite laminates with a hole by using peridynamic theory," in *Proceedings of 54th AIAA/ASME/ASCE/AHS/ASC Structures, Structural Dynamics, and Materials Conference*, Boston, MA, USA, April 2013.
- [30] K. Colavito, *Peridynamics for failure and residual strength prediction of fiber-reinforced composites*, Ph.D. thesis, University of Arizona, Tucson, Arizona, 2013.
- [31] E. Madenci and E. Oterkus, *Peridynamic Theory and Its Applications*, Springer, New York, NY, USA, 2014.
- [32] B. Kilic and E. Madenci, "An adaptive dynamic relaxation method for quasi-static simulations using the peridynamic theory," *Theoretical and Applied Fracture Mechanics*, vol. 53, no. 3, pp. 194–204, 2010.
- [33] M. Fatica and G. Ruetsch, *CUDA Fortran for Scientists and Engineers: Best Practices for Efficient CUDA Fortran Programming*, ELSEVIER, Amsterdam, Netherlands, 2013.
- [34] P. P. Camanho, P. Maimí, and C. G. Dávila, "Prediction of size effects in notched laminates using continuum damage mechanics," *Composites Science and Technology*, vol. 67, no. 13, pp. 2715–2727, 2007.

